Hambal Tella
Graduate Student, King Fahd University of Petroleum and Minerals, Electrical Engineering Department, Saudi Arabia

Mohamed A. Mohandes
Professor
King Fahd University of Petroleum and Minerals, Electrical Engineering Department
Saudi Arabia

B. Liu
Assistant Professor
King Fahd University of Petroleum and Minerals, Electrical Engineering Department
Saudi Arabia

Ali Al-Shaikhi
Associate Professor
King Fahd University of Petroleum and Minerals, Electrical Engineering Department
Saudi Arabia

Shafiqur Rehman
Associate Professor
King Fahd University of Petroleum and Minerals, Electrical Engineering Department
Saudi Arabia

A Novel Cost-Function for Transformer-based YOLO Algorithm to Detect Photovoltaic Panel Defects

Solar panel defects can lead to substantial efficiency loss and increased maintenance expenses. Conventional defect detection methods are often slow and ineffective. Thisstudy revisits the You Only Look Once (YOLO) algorithm and its variations, assessing their efficacy in identifying defects in thermal images of solar panels. Subsequently, we introduce a novel YOLO algorithm, termed YOLOS-PV, built uponthe transformer-based YOLOS algorithm. The proposed algorithm introduces newloss function weights to prioritize localized objects and visualize the attention mapof each transformer head within the YOLOS algorithm. In the experiments, theYOLOS-PV achieves a mAP@0.5:0.95 score of 0.894, surpassing the efficiency ofother YOLO variants. Code implementation can be found here: tella26/YOLOS-PV (github.com)

Keywords: *Solar panels, defect detection, deep learning, YOLO models, cost function*

1. INTRODUCTION

Rapid population growth and drastically increasing power requirements are critical concerns to address the energy needs [1,2]. However, traditional power plants cannot be built to meet the pace of increasing energy demands [3]. Solar power plants consist of numerous Solar Panels (SPs) organized in arrays ona supportive framework [4]. These panels can be installed on buil–ding rooftops orfacades to supply electricity to the buildings [5]. However, the outdoor arrangementof the SPs exposes them topotentially harsh conditions, which can adversely affect their performance and lead to defects. These defects mayinclude hotspots [6], cracks and corrosion [7], broken glass [8], and others, as outlined in Table 1.

Detecting defective solar panels has traditionally reliedon experts, who, thoughreliable,can be inefficient [9]. Moreover, conventional methods like thermal and electricalmodeling [10], which primarily analyze tem–perature and power output to assess performance, often fall short in detecting defects such as cracks orhotspots [11]. Optimal utilization of renewable energy systems depends on the harmonization of various processes like design, manufacturing, materials, technology, policy and regulations, standards, and testing [2, 12-15]. To overcomethese constraints, a combination of imaging techniques, including Electroluminescence (EL), Infra-Red Thermography (IRT) [16], Lock-in Thermography (LIT) [17], Ultraviolet (UV) [18], Magnetic Field Ima–ging (MFI) [19], and Spectroscopic Diagnostic Techni–ques (SDT) [20], along with classification techniques like Wavelet Transform andFast Fourier Transform (FFT) [21], have been proposed. Deep Learning (DL) [22] hasemerged as a promising approach for effectively identifying defects in solar panels, defect visibility, and efficient localization. Our survey of related models concerning solar panel defect detection revealed that RGB images are not suitable for the visibility of defects [23]. This is why nondestructive detection techniques, such as IRT, LIT, etc., are applied before the object detection process. These techniques ensure enhanced facilitating more accurate defect detection and classi–sfication.

Table 1. Type of defects in solar modules caused by the manufacturer, environmental conditions, and users.

No	Defect Type	Causes
1	Hotspot [6]	Extreme Temperature
2	Broken glass [8]	Hail or collisions
3	Dust Build up	Strong wind or dust accumulation
4	Cracked back sheets	Collision or other harsh environmental conditions
5	Ribbon Discoloration	Corrosion, heat, or moisture exposure
6	Encapsulant Discoloration	UV light exposure, high temperature, and humidity
7	Delamination	Manufacturing, installation issues, Environmental conditions, etc.
8	Bubbles	Inadequate heating and moisture or contaminants
9	Defective Junction box [24]	Faulty connections
10	Potential Induced Degradation (PID)	Exposure to high temperatures and humidity

Received: July 2024, Accepted: October 2024
Correspondence to: Prof. Shafiqur Rehman, Electrical Engineering Department, King Fahd University of Petroleum & Minerals (KFUPM), Dhahran, Saudi Arabia, E-mail: srehman@kfupm.edu.sa
doi: 10.5937/fme2404639T

11	Corroded [25]	Moisture or humidity and extreme temperature
12	Soiling	Accumulation of dirt, dust, or other materials
13	Diode Defects [26]	Installation and functioning of bypass diodes

IRT is a nondestructive imaging technique that preserves the integrity of the captured sample image. It utilizes infrared radiation to capture and generate an image of solar panels to depict their temperature distri–bution. Figure 1 illustrates examples of solar thermal images [27].

You Only Look Ones (YOLO) is one of the most important object detection algorithms [28]. YOLOv3 is applied in [29] to Infra-Red (IR) and RGBdataset collected by a drone, and the same model is applied in 30] to only IR images. The IR images are used for hotspot defects, while the RGB images are for other defects.YOLOv3 gives mAP@0.5 of 0.70 and a 74% confidence level for the hotspot test images. Also, [31] proposed a TPH-YOLOv5 model that is based on the YOLOv5 by replacing the prediction heads with Transformer Prediction Heads (TPH) [32]. However, this model is used on drone-based RGB datasets, which gives an average precision of about 39%.

Likewise, a faster Region-based Convolutional Neural Network (RCNN) model[33], known as edge detection algorithms, was used to localize hotspot defects on IR thermal images. This method achieved anmAP of 0.67. The YOLOv5 model was used in [34] by improving the anchor boxes and prediction heads of the algorithm, which is termed AP-YOLOv5. This achievedanmAP of 0.87, an average recall of 89.00%, and an F1 score of 88.90% on IR thermal images.Our work focuses on improving the detection and localization of solar panel defects by bridging the gap of past works. Specifically, we evaluated the performance of six YOLO variants, namely, YOLOv5 and YOLOv5-OBB [35], YOLOv6 [36], YOLOv7 [37], YOLOv8 [38], and YOLOS [39], and developed a YOLOS-PV based on the transformer YOLOS object detection model. The proposed algorithm outperforms the other tested YOLO variants.

Table 2. Summary of surveyed papers.

Authors	Model	Dataset(s)	Results
Tommaso *et al.* [29]	YOLOv3	Infra-red imaging by Drone (Unavailable)	0.70(mAP@0.5)
Tajwar *et al.*[30]	YOLOv3	Thermal images (Unavailable)	74.00% (Acc)
Zhu *et al.* [31]	TPH-YOLOv5	VisDrone2021, DET-test-challenge (Available)	DET 39.18% (AP) and Vis 39.43% (AP)
Pathak *et al.* [33]	faster RCNN	IR thermal Image (Unavailable)	0.67 (mAP)
Sun *et al.*[34]	YOLOv5	IR thermal Image (Unavailable)	87.80%(mAP), 89.00% (AR)

Figure 1. Typical solar panel cell defect detection

2. METHODOLOGY

2.1 Dataset Description

A comprehensive dataset is crucial to developing and training effective DL models for SP defect detection. In this section, we elaborate on how the dataset was collected and preprocessed. While most datasets used in the literature for SP defect detection are RGB, we opted for solar thermal image datasets in this research. This decision stems from the observation that defect detection in RGB images often misclassifies functional SPs as defective, as depicted in Figure 2. We collected a dataset that comprises 1,056 high-resolution 640 × 640 images captured using a thermal camera across various solar panel environments, and a sample is shown in Figure 1. Each image is annotated with binding boxes and defect class labels following the Common Objects in Context (COCO) dataset format. These solar thermal images were gathered from companies that made datasets publicly available, such as Nanonets[40] and Roboflow[41]. Additionally, we have used samples from a local solar plant in SAKAKA, Saudi Arabia.

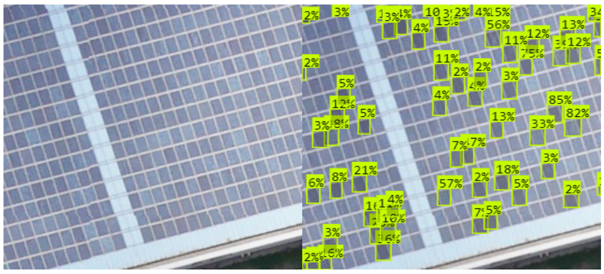

Figure 2. RGB image of solar panels and falsely detected Defects.

2.2 Defect Localization using YOLO Models

We experimented with variants of YOLO algorithms, including YOLOv5, YOLOv5-OBB, YOLOv6, YOLOv7, YOLOv8, and YOLOS. We found that YOLOS performed better than the other variants. YOLOS is an object detection model based on the vanilla Vision Transformer (ViT)[42] with Sequential Positional Encoding (SPE)[43]. Unlike previous mo–dels, YOLOS uses a ViT block as its backbone. The architecture of YOLOS consists of several layers of SPE blocks, followed by a transformer encoder block. The SPE blocks encode spatial and sequential information about the image features, while the encoder helps the model to learn contextual relationships between features.

The process takes a single 640 × 640 thermal image, which is converted into 16×16of 40 image patches, where time variability is not considered. These sets of image patches as tokens and a corresponding set of positional embedding, also referred to as “queries,” are then passed as inputs to the transformer block encoder, as shown in Figure 3.

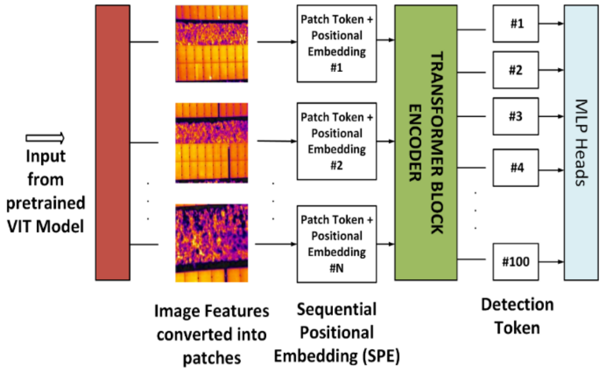

Figure 3. A diagram of the YOLOS model on object detection for solar images

The pre-trained ViT model used in YOLOS is adapted from the transformer architecture and was initially designed for natural language processing and visual data processing. It divides an input image into a sequence of smaller patches, linearly embeds them, and passes them through multiple layers of self-attention mechanisms to capture relationships between patches. The ViT model used in YOLOS has been pre-trained on large datasets such as ImageNet, which consists of over 14 million images. This pre-training allows it to learn general visual features and patterns, making it effective for various downstream tasks. The Multilayer Percep–tron (MLP) heads help to fuse the detection token pro–duced from the output of the transformer encoder to give the defect classification and bounding box predic–tions [44]. Figure 4. shows the overall system, including the pre-trained ViT module. The matching process of the objects uses the following global loss function,

$$\mathcal{L}_{YOLOS} = \lambda_{loc}\mathcal{L}_{loc} + \lambda_{obj}\mathcal{L}_{obj} + \lambda_{cls}\mathcal{L}_{cls} \tag{1}$$

where λ_{loc}, λ_{obj}, λ_{cls} and represent the weights assigned to the localization, objectness, and classification loss ter–ms, respectively. $\mathcal{L}_{loc}$ measures the error of the pre–dicted bounding box locations, $\mathcal{L}_{obj}$ measures the error of the predicted object, and $\mathcal{L}_{cls}$ measures the error of the predicted class label.

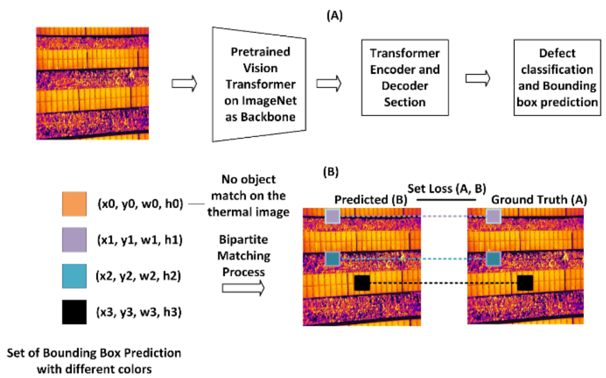

Figure 4. The overall detection system with the ViT module.

The commonly used Intersection over Union (IoU) loss is a measure of dissimilarity between two bounding boxes. Let B_{pred} be the predicted bounding box and B_{gt} be the ground truth bounding box. The IoU of B_{pred} and B_{gt} is defined as:

$$IoU\left(B_{pred}, B_{gt}\right) = \frac{\left(B_{pred} \cap B_{gt}\right)}{\left(B_{pred} \cup B_{gt}\right)} \tag{2}$$

where $B_{pred} \cap B_{gt}$ is the overlapped area of these two boxes, as exhibited with the shaded rectangle in the left panel of Figure 4. Meanwhile, $B_{pred} \cup B_{gt}$ is the union of these two bounding boxes, as shown in the right panel of Figure 5. However, IoU is zero when no over–lapping area exists between B_{pred} and B_{gt}. See Figure 5 for example. Therefore, we have modified IoU to a mo–re general metric Generalized IoU (GIoU) as follows,

$$GIou\left(B_{pred}, B_{gt}\right) = IoU\left(B_{pred}, B_{gt}\right) - \frac{\left(en-box\left(B_{pred}, B_{gt}\right) - B_{pred} \cup B_{gt}\right)}{en-box(B_{pred}, B_{gt})} \tag{3}$$

where $en-box(B_{pred}, B_{gt})$ is the smallest bounding box enclosing both B_{pred} and B_{gt}. The GIoU metric considers both overlap and structural differences between the two areas as it adds structural similarity to the overlap mea–surement IoU, as shown in Figure 6. The total GIoU loss for all N objects in an image can be expressed as follows,

$$GIou\ Loss = \left(\frac{1}{N}\right)\sum_{i=1}^{N}\left(1 - GIoU\left(b_i, \hat{b}_i\right)\right) \tag{4}$$

Here, b_i is the ground truth bounding box for the *ith* object in the image, $\hat{b}_i$ is the predicted bounding box for the object, $GIoU\left(b_i, \hat{b}_i\right)$ is the GIoU between b_i and $\hat{b}_i$.

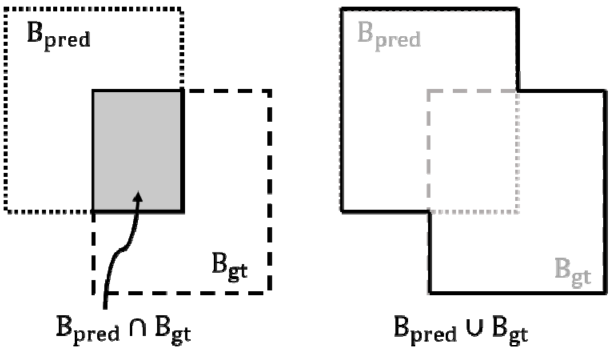

Figure 5. The overlapping, union, and the en-box of two bounding boxes

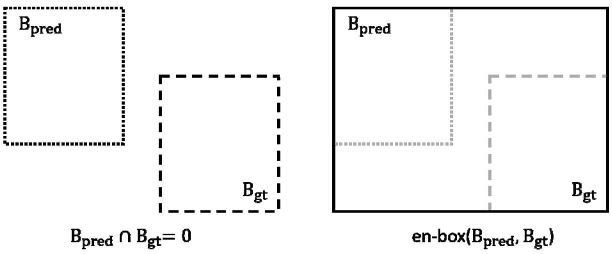

Figure 6.The overlapping, union, and the en-box of two bounding boxes.

The Detection Transformer (DETR) model is popu–larly known as End-to-End Object Detection with

Transformers [45]. It uses a unique loss function called Set Prediction Loss, which aims to solve the object detection problem as a set prediction task rather than a region proposal problem. The loss function includes two terms: Binary Cross-Entropy (BCE) Loss and Set Loss. BCE measures the loss for object predictions (whether an object is present in a particular class). In contrast, set loss measures the matching between predicted and ground-truth object sets using a bipartite matching process. The corresponding equation for the BCE loss is:

$$WeightedL_{box\left(b_i,\hat{b}_{\sigma(i)}\right)} = W_{GIoU} \cdot \lambda_{GIoU}\left(b_i,\hat{b}_{\sigma(i)}\right) + W_l^1 \cdot \lambda_l^1 \left\| b_i - \hat{b}_{\sigma(i)} \right\|_1 \tag{5}$$

where vector y = [y_1, y_2, …, y_N] represents the ground truth binary labels (0 or 1) for the N samples, vector $\hat{y} = \left[\hat{y}_1, \hat{y}_2, ..., \hat{y}_N\right]$ represents the predicted probabilities for the positive class, and log(·) is the natural logarithm function. The Set Loss is given by:

$$SetLoss(A,B) = BCELoss\left(C(A)\hat{C}(B)\right) + \lambda \cdot L_{box}\left(L(A),\hat{L}(B)\right) \tag{6}$$

where A is the ground-truth object set, B is the predicted object set; C(A) is the binary mask indicating the presence or absence of objects, $\hat{C}(B)$ is the predicted mask, L(A) is the ground-truth bounding box location matrix, $\hat{L}(B)$ is the predicted matrix, and λ is a balancing hyperparameter. L(A) and $\hat{L}(B)$ are matrix combinations of b_i and $\hat{b}_\sigma(i)\ \hat{b}_i$, respectively. L_{box} is a linear combination of GIoU and l_1 regression loss shown as follows,

$$L_{box} = (b_i,) = \lambda \cdot GIoU\left(b_i, \hat{b}_\sigma(i)\right) + +\lambda_{L_1} \cdot \left\| b_i - \hat{b}_\sigma(i) \right\|_1 \tag{7}$$

where b_i denotes the i-th object, and $\hat{b}_\sigma(i)$ denotes the prediction with the lowest cost from b_i in terms of Hungarian algorithm-based matching loss [45]. $\Lambda_{GIoU} \in R$ and $\Lambda_{L_1} \in R$ are hyperparameters that cont–rol the weighting of the GIoU Loss component and the l_1 regression loss in the overall loss function. The authors of DETR suggested $\lambda_{\text{GIoU}} = 5$ and $\lambda_{\text{L1}} = 1$, [46]. Notation $\left\| b_i - \hat{b}_\sigma(i) \right\|_1$ denotes the l_1 norm. The losses are normalized by the number of objects in the batch.

l_1 loss in YOLOS Models

In YOLOS, the l_1 loss is used to measure the difference between the predicted bounding box coordinates and the ground-truth bounding box coordinates. Suppose we have N ground-truth objects in an image; then the predicted bounding box coordinates and sizes for each of these objects are denoted as (x_i, y_i, w_i, h_i), i = 1,2, …N, where coordinate (x_i,y_i) denotes the center of the i-th box, and the pair (w_i, h_i) hi represent the width and height of the same box, respectively. Similarly, the ground-truth bounding box coordinates and sizes are denoted as (x_{i0}, y_{i0}, w_{i0}, h_{i0}). The l_l loss for a single object i is defined as the sum of the absolute differences between the predicted and ground-truth bounding box coordinates and sizes:

$$L_{l_1}(i) = |x_i - x_{i0}| + |y_i - y_{i0}| + |w_i - w_{i0}| + |h_i - h_{i0}| \tag{8}$$

The total l_1 loss for all N objects in an image is obtained by summing up the loss over all objects.

$$L_{l_1} = \sum_{i=1}^{N} L_{l_1}(i) \tag{9}$$

Weighted GIoU and l_1 losses for YOLOS-PV

A linear combination of GIoU and l_1 losses in equation (7) is inefficient for some problems. This was proposed by [46] to solve the problem of different scales for small and large boxes, even if their relative errors were similar. However, defect localization in the solar panels using the YOLOS algorithm with the linear combination of losses results in ineffective bounding box predictions of the defects during the inference. This sometimes results in overlapping of the bounding boxes of different class scores on the same object. However, using a weighted loss combination ensures assigning more priority to any of the GIoU or l_1 loss, which helps suppress an unwanted bounding box loss.We introduce two hyperparameters, i.e., W_{GioU} and W_{l1}, as the weights of GIoU Loss and l_1-Loss, respectively,

$$FinalWeightLoss = W_{GIoU} \cdot GIoULoss + W_{l_1} \cdot L_{l_1} \tag{10}$$

where the sum of W_{l1} and W_{GioU} is always equal to 1. Rewriting the equation yields:

$$WeightedL_{box\left(b_i,\hat{b}_{\sigma(i)}\right)} = W_{GIoU} \cdot \lambda_{GIoU}\left(b_i,\hat{b}_{\sigma(i)}\right) + W_l^1 \cdot \lambda_l^1 \left\| b_i - \hat{b}_{\sigma(i)} \right\|_1 \tag{11}$$

3. EXPERIMENTAL RESULTS

3.1 Solar Panel Defect Localization Results

Before discussing the results, we will briefly explain the performance measures that we have used. In object detection, Mean Average Precision (mAP) is used as an algorithm performance measure. Precision measures how accurate the algorithm's predictions are. i.e., the number of correct detections that the system finds (true positive) is divided by the total number of detections that the system finds (true positive + false positive). Object detection systems make predictions in terms of a bounding box of the detected object. For each bounding box, we measure an overlap (intersection) between the predicted bounding box and the ground truth bounding box. This is used by the IoU explained above. A threshold value is pre-selected; if the IoU exceeds this specified value, it leads to a true object being detected. The mAP is calculated by taking the mean AP over all IoU thresholds.

Another important performance measure is the Recall. It measures how well the system finds all positives, i.e., the number of correct detections that the system finds (true positive) divided by the total number of existing true objects (true positive+false negative). The Mean Average Recall (mAR) is the recall averaged over all IoU thresholds between 0.5 and 1.0. More details about the mAP and mAR and their calculations can be found in [47,48].

We experimented on the six YOLO variants inclu–ding YOLOv5, YOLOv5-OBB, YOLOv6, YOLOv7, YOLOv8 and YOLOS for 100 epochs. The batch size is16, the image resolution is 640, the learning rate is 2.5e-5, and the weight decay is 1e-4. The experimental results are displayed in Table 3, where symbol + indi–cates that the modelis used on a different dataset. The results show the transformer-based YOLOS algorithm has better mAP@0.5:0.95 of the value 0.867 and mAR@0.5:0.95 of the value 0.952. The metric mAP@0.5 measures the ave–rage precision when the IoU threshold is set to 0.50, while mAP@0.5:0.95 measures the average precision when the IoU threshold is varied from 0.50 to 0.95 with a step of 0.05. The range specifies that the AP is calculated at ten different IoU thresholds, ranging from 0.50 to 0.95. A value of 1.0 for mAP@0.5 indicates perfect perfor–mance, while a 0.0 means the model fails to detect any defects. In our case, we got a value of 0.867, which indi–cates that YOLOS can detect around 86.70% of the def–ects in the test set correctly out of the ten different IoU thresholds.

Table 3. Experimental results of YOLO variants on object detection.

Models	Precision	Recall	mAR @0.5:0.95	mAP @0.5	mAP @0.5:0.95
Tommaso (Yolov3) [29]+	-	-	-	0.700	-
Zhu (TPH-YOLOv5) [31]+	-	-	-	-	0.394
Pathak (faster RCNN) [33]+	-	-	-	-	0.670
Sun (YOLOv5) [34] +	-	-	0.890	-	0.878
YOLOv5 [35]	0.692	0.491	-	0.511	0.258
YOLOv5-OBB [35]	0.637	0.371	-	0.411	0.153
YOLOv6 [36]	-	-	0.835	0.483	0.767
YOLOv7 [37]	0.805	0.769		0.796	0.370
YOLOv8 [38]	0.715	0.691		0.752	0.463
YOLOS [39]	-	-	0.952*	0.335	0.867
YOLOS-PV (Ours)*	-	-	0.952*	0.335	0.894*

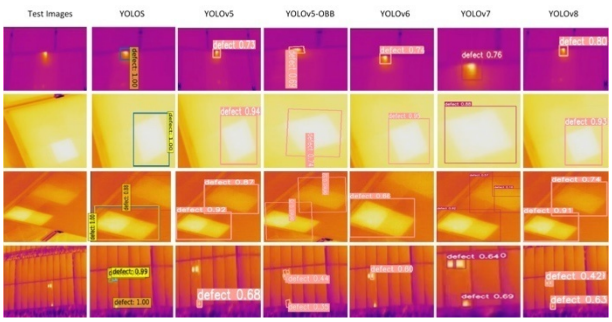

Figure 7. Inference experimental results on solar thermal images using six YOLO variants.

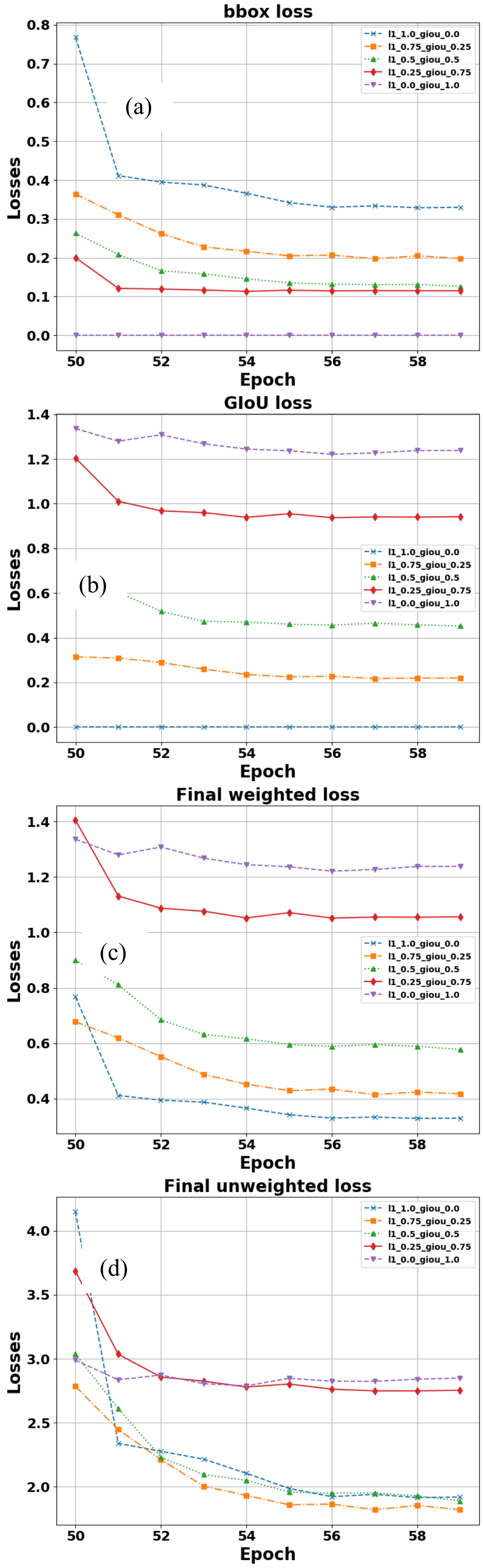

Figure 8. Results of varying the weighted hyperparameters of W_{l1} AND W_{GIoU} with the l_1 and giou loss for the defects localization in solar thermal images. a weight of l_1 = 0.250 and giou = 0.750 gives a better loss combination for the selected learning rate of 2.5e-5. this gives a final giou loss of 0.970, a final weight loss of 1.100 during training, and a test loss value of 2.890 within the 10 epochs window from 50 to 59 epoch.

Similarly, we evaluate each model on the inference dataset as shown in Figure7.The figure shows four rows of different input IR images (left) and the results of defects detections by the 6 YOLO variants. For each algorithm the figure shows the detected objects (in this case it is the defects), the bounding box, and the confi–dence score of the detection. The performance of each model is zoomed-in for a better score display. One can easily observe that the YOLOS transformer model has confidence levels close to 1.0 for most detected defects compared to the other variants. Itis concluded that the YOLOS model has better inference performance but with overlapping bounding box prediction in some cases.

3.2 YOLOS-PV weighted loss results

In this section, we implemented the proposed YOLOS-PV method on the same dataset used in the previous experiment. We vary the values of the weights W_{l1} and W_{GIoU} from 0 to 1 in steps of 0.25 while both weights added to 1. We evaluate our results in a window of 10 epochs from 50 to 59 epochs. The results, as visualized in Figure 8, show that for the problem of localizing defects in solar thermal images, the best combination of the effective weight is $W_{l1} = 0.25$ and $W_{GIoU} = \mathbf{0.75}$.

According to[49], the combination above results in a suitable learning rate as compared with other combi–nations. The most similar combination is $W_{l1} = \mathbf{1}$ and $W_{GIoU} = \mathbf{0}$, which totally shuts down the effect of GIoU loss. However, this means that the bounding boxes overlap even more and the effect of the GIoU loss is removed. Since GIoU loss helps measure the dissimi–larity between two bounding boxes and consider the overlap, we selected the 0.25 and 0.75 weight combi–nations for the YOLOS-PV model. This configuration is then trained on the images with the same hyper–parameters chosen for the other models. This improves the mAP@0.5:0.95 to 0.894 as shown in Table 3.

4. CONCLUSION

In this paper, we introduced the YOLOS-PV model, which is based on the transformer YOLOS model. Initially, we applied six state-of-the-art YOLO variants, i.e., YOLOv5, YOLOv5-OBB, YOLOv6, YOLOv7, YOLOv8, and YOLOS, to localize defect class objects on the solar panels. Among these models, the YOLOS model demon–strated superior performance with a mAP@0.5:0.95 score of 0.867. To enhance the localization and bounding boxprediction accuracy of solar thermal images, we proposed YOLOS-PV by introdu–cing hyperparameter weighted values to the linear com–bination of bounding box loss, comprising l_1 regression loss and GIoU loss. This approach grants us greater control in adjusting the effectiveness of the loss function. Through experimen–tation, we determined that setting $W_{l1} = \mathbf{0.250}$ and WGIoU = **0.750** yielded optimal weight combinations for defect localization in solar thermal images.

5. FUTURE DIRECTION

One potential area for improvement is to further study the variation of defects in different solar panel plants, such as hotspots, diodes, and junctions unlike using one class. This would require collaboration with the industry to obtain more accurate and comprehensive data, which can be used to refine the algorithms and improve the detection performance. Another area for improvement is the optimization of the weight values of l_1 and GIoU during training, using optimization techniques such as gradient descent. This can potentially lead to better localization accuracy and faster convergence during training. Finally, an interesting future direction would be to apply and fine-tune the weights hyperparameters to other domains apart from defect classification of solar thermal images, which could include other types of imaging modalities or even non-imaging data. This would require further research and experimentation to determine the applicability and effectiveness of the transformer-based YOLOS-PV algorithm in different domains.

ACKNOWLEDGMENT

The authors acknowledge the support of KFUPM and SDAIA under grant number JRC-AI-UCG-03.

REFERENCES

[1] B. Rašuo, A. Bengin, A. Veg, “On Aerodynamic Optimization of Wind Farm Layout,” PAMM Proc. Appl. Math. Mech., vol. 10, no. 1, pp. 539–540, 2010. Doi: 10.1002/pamm.201010262

[2] B. Rašuo, M. Dinulović, A. Veg, A. Grbović, A. Bengin, “Harmonization of new wind turbine rotor blades development process: A review, Renew. Sustain. Energy Rev., vol. 39, pp. 874–882, 2014. doi: 10.1016/j.rser.2014.07.137

[3] B. P. Rašuo and A. Bengin, “Optimization of wind farm layout,” FME Trans., vol. 38, no. 3, pp. 107–114, 2010.

[4] Electrical Technology. "How a Photovoltaic Power Plant Works? Construction and working." 2021. Available at:https://www.electricaltechnology.org/2021/07/solar-power-plant.html. [Accessed July 2024]

[5] Kalogirou, Soteris. "Building Integration of Solar Renewable Energy Systems Towards Zero or Nearly Zero Energy Buildings." International Journal of Low-Carbon Technologies, 2013. doi:10.1093/ijlct/ctt071.

[6] Meyer, S., Richter, S., Timmel, S., Gläser, M., Werner, M., Swatek, S., Hagendorf, C. "Snail Trails: Root Cause Analysis and Test Procedures." Energy Procedia, vol. 38, 2013, pp. 498-505. doi:10.1016/j.egypro.2013.07.309.

[7] Carlson, D.E., Romero, R., Willing, F., Meakin, D., Gonzalez, L., Murphy, R., Moutinho, H.R., and Al-Jassim, M. "Corrosion Effects in Thin-Film Photo–voltaic Modules." Prog. Photovolt: Res. Appl., vol. 11, 2003, pp. 377-386. doi:10.1002/pip.500.

[8] Bouraiou, A., Hamouda, M., Chaker, A., Neçaibia, A., Mostefaoui, M., Boutasseta, N., Ziane, A., Dabou, R., Sahouane, N., Lachtar, S. "Experimental Investigation of Observed Defects in Crystalline

Silicon PV Modules Under Outdoor Hot Dry Cli–matic Conditions in Algeria." Solar Energy, vol. 159, 2018, pp. 475-487. doi: 10.1016/j.solener. 2017.11.018.

[9] Al-Waisy, A. et al. "Identifying Defective Solar Cells in Electroluminescence Images Using Deep Feature Representations." PeerJ Computer Science, 2022. doi:10.7717/peerj-cs.992.

[10] Elyaqouti, M., et al. "Thermal and Electrical Modeling of Photovoltaic Modules." International Journal of Ambient Energy, vol. 43, 2021, pp. 1-41. doi:10.1080/01430750.2021.1994464.

[11] Sohani, A., et al. "Using Machine Learning in Pho–tovoltaics to Create Smarter and Cleaner Energy Generation Systems: A Comprehensive Review." Journal of Cleaner Production, vol. 364, 2022, p. 132701. doi:10.1016/j.jclepro.2022.132701.

[12] Dinulović, M. R., Trninić, M. R., Rašuo, B. P., and Koźović, D. V.: Methodology for aero-acoustic noise analysis of 3-bladed h-Darrieus wind turbine, Thermal Science, Vol. 27 (1 Part A), pp. 61-69, 2023. https://doi.org/10.2298/TSCI2301061D

[13] Rašuo, B. P., Veg, A. D.: Design, fabrication, and verification testing of the wind turbine rotor blades from composite materials, in: Proceedings of the ICCM-16, Japan, 2007, pp. 1-4.

[14] Parezanovic, V., Rašuo, B., Adzic, M.: Design of airfoils for wind turbine blades. in: Proceedings of the French-Serbian European Summer University: Renewable Energy Sources and Environment-Multidisciplinary Aspect, 2006, pp. 195-200.

[15] Rašuo, B., Bengin, A., Dinulović, M., Grbović, A.: Development of new optimal adapttronic airfoils, using modern engineering software packages, Tehnika, vol. 79, iss. 3, pp. 305-321, 2024. doi: 10.5937/tehnika2403305R

[16] Jahn, Ulrike, Magnus Herz. Review on Infrared and Electroluminescence Imaging for PV Field Applications. IEA International Energy Agency, 2018. ISBN 978-3-906042-53-4.

[17] Besold, S., Hoyer, U., Bachmann, J., et al. "Quanti–tative Imaging of Shunts in Organic Photovoltaic Modules using Lock-in Thermography." Solar Energy Materials and Solar Cells, vol. 124, 2014, pp. 133-137. doi:10.1016/j.solmat.2014.01.030.

[18] Sulas-Kern, D. B., et al. "UV-Fluorescence Imaging of Silicon PV Modules After Outdoor Aging and Accelerated Stress Testing." In 47th IEEE Photo–voltaic Specialists Conference (PVSC), 2020.

[19] Paduthol, A., et al. "Magnetic Field Imaging: Strengths and Limitations in Characterising Solar Cells." In IEEE 46th Photovoltaic Specialists Conference (PVSC), 2019.

[20] Czirjak, A. "Investigation of the Spectral Properties of Photovoltaic Modules using Spectroscopy." *WIT Transactions on Ecology and the Environment*, vol. 251-260, 2017, p. 219.

[21] Perarasi, M., GeethaRamadas, N. "Detection of Cracks in Solar Panel Images Using Complex Wavelet Transform and ANFIS Classification Method." doi:10.21203/rs.3.rs-924118/v1.

[22] [Tang, W., et al. "Deep Learning Based Automatic Defect Identification of Photovoltaic Module using Electroluminescence Images." *Solar Energy*, vol. 201, 2020, pp. 453-460. doi:10.1016/j.solener.2020 .03.049.

[23] Li, X., Yang, Q., Chen, Z., Luo, X., Wenjung, Y. "Visible Defects Detection Based on UAV-Based Inspection in Large-Scale Photovoltaic Systems." IET Renewable Power Generation, vol. 11, 2017. doi:10.1049/iet-rpg.2017.0001.

[24] Lausch, D., Patzold, M., Rudolph, M., Lin, C.-M., Fröbel, J., Kaufmann, K. "Magnetic Field Imaging (MFI) of Solar Modules." 35th European Photo–voltaic Solar Energy Conference and Exhibition (EUPVSEC), 2019, pp. 1060-1064. doi:10.4229/ 35th EUPVSEC20182018-5BO.11.5.

[25] Elgharbawy, Abdallah S. "Review on Corrosion in Solar Panels." International Journal of Smart Grid, 2018. Available at: https://api.semanticscholar.org/ CorpusID:134763725.

[26] Dhimish, Mahmoud, et al. "Detecting Defective Bypass Diodes in Photovoltaic Modules using Mamdani Fuzzy Logic System." Global Journal of Research in Engineering, 2017, pp. 33-44.

[27] elpv-dataset. Available at https://github.com/zae-bayern/elpv-dataset].[Accessed 5 October 2024].

[28] Object Detection with Yolo: Hands-on Tutorial. Available at https://neptune.ai/blog/object-detection -with-yolo-hands-on-tutorial. A variant of this algorithm [Accessed 5 October 2023].

[29] Di Tommaso, A., Betti, A., Fontanelli, G., Michelozzi, B. "A Multi-Stage Model Based on YOLOv3 for Defect Detection in PV Panels Based on IR and Visible Imaging by Unmanned Aerial Vehicle." Renewable Energy, vol. 193, 2022, pp. 941-962. doi: 10.1016/j.renene.2022.04.046.

[30] Tajwar, T., Hassan Mobin, O., Khan, F. R., Hossain, S. F., Islam, M., Mosaddequr Rahman, M. "Infrared Thermography Based Hotspot Detection of Photovoltaic Module Using YOLO." In 2021 IEEE 12th Energy Conversion Congress & Expo–sition - Asia (ECCE-Asia), Singapore, 2021, pp. 1542-1547. doi:10.1109/ECCE-Asia49820.2021. 9478998.

[31] Zhu, X., Lyu, S., Wang, X., Zhao, Q. "TPH-YOLOv5: Improved YOLOv5 Based on Transfor–mer Prediction Head for Object Detection on Drone - Captured Scenarios." In 2021 IEEE/CVF Inter–national Conference on Computer Vision Work–shops (ICCVW), Montreal, BC, Canada, 2021, pp. 2778-2788. doi:10.1109/ICCVW54120.2021.00312.

[32] Tutorial 14: Transformers I: Introduction. Available at https://www.borealisai.com/research-blogs/tuto–rial-14-transformers-i-introduction/. [Accessed 5 October 2024].

[33] Pathak, S.P., Patil, S., Patel, S. "Solar Panel Hotspot Localization and Fault Classification Using Deep Learning App–roach." Procedia Computer

Science, vol. 204, 2022, pp. 698-705. doi:10.1016/ j.procs.2022.08.084. Available at: https://doi.org/ 10.1016/j.procs.2022.08.084.

[34] Sun, T., et al. "A Novel Detection Method for Hot Spots of Photovoltaic (PV) Panels Using Improved Anchors and Prediction Heads of YOLOv5 Network." *Energy Reports*, vol. 8, 2022, pp. 1219-1229. doi:10.1016/j.egyr.2022.08.130. Available at: https://doi.org/10.1016/j.egyr.2022.08.130.

[35] "YOLOv5: The Friendliest AI Architecture You'll Ever Use." Ultralytics, 2020. Available at: https://ultralytics.com/yolov5. [Accessed 8 April 2023].

[36] Li, Chuyi, et al. "YOLOv6: A Single-Stage Object Detection Framework for Industrial Applications." 2022. doi:10.48550/arXiv.2209.02976.

[37] Wang, Chien-Yao, Bochkovskiy, Alexey, and Liao, Hong-yuan. "YOLOv7: Trainable Bag-of-Freebies Sets New State-of-the-Art for Real-Time Object Detectors." 2022. doi:10.48550/arXiv.2207.02696.

[38] Ultralytics. Ultralytics YOLOv8: The State-of-the-Art YOLO Model, 2023. Available at: https:// ultralytics.com/yolov5. [Accessed 8 April 2023].

[39] Fang, Yuxin, et al., You Only Look at One Sequence: Rethinking Transformer in Vision thro–ugh Object Detection, 2021. doi:10.48550/ arXiv. 2106.00666.

[40] Solar Plant Inspection, 2023. Available at: https:// nanonets.com/drone/solar-panels/. [Accessed April 2023].

[41] The World's Largest Collection of Open-Source Computer Vision Datasets and APIs,Roboflow Universe, 2023. Available at: https://universe. roboflow.com/. [Accessed April 2023].

[42] “Vision Transformer: What It Is and How It Works”, Available at https://www.v7labs.com/blog /vision-transformer-guide. [Accessed 5. 10. 2024].

[43] “A Gentle Introduction to Positional Encoding in Transformer Models”, Available at https://machine learningmastery.com/a-gentle-introduction-to-positi onal-encoding-in-transformer-models-part-1/. [Accessed 5 October 2024].

[44] “An Overview on Multilayer Perceptron (MLP)”, Available at https://www.simplilearn.com/tutorials/ deep-learning-tutorial/multilayer-perceptron. [Ac–cessed 5 October 2024].

[45] Stewart, R. J., Andriluka, M., Ng, A. Y. "End-to-End People Detection in Crowded Scenes." In *IEEE Conference on Computer Vision and Pattern Recognition (CVPR)*, 2015.

[46] Carion, N., Massa, F., Synnaeve, G., Usunier, N., Kirillov, Aand Zagoruyko, S. "End-to-End Object Detection with Transformers." In *Computer Vision – ECCV 2020*, 2020. doi:10.1007/978-3-030-58452-8_13.

[47] Mean Average Precision (mAP) Explained: Every–thing You Need to Know. Available at https:// www.v7labs.com/blog/mean-average-precision. [Accessed 5 October 2024].

[48] Calculating mean Average Recall (mAR), mean Average Precision (mAP). Available at https:// github.com/matterport/Mask_RCNN/issues/2513. [Accessed 5 October 2024].

[49] CS231n Convolutional Neural Networks for Visual Recognition, Stanford University. "Loss Function." Available at: https://cs231n.github.io/neural-net–works-3/#loss. [Accessed 28 July 2024].

НОВА ФУНКЦИЈА ТРОШКОВА ЗА YOLO АЛГОРИТАМ ЗАСНОВАН НА ТРАНС–ФОРМАТОРУ ЗА ОТКРИВАЊЕ ДЕФЕКАТА ФОТОНАПОНСКИХ ПАНЕЛА

М. Тела, М.А. Мохандес, Б. Лиу, А. Ал-Шаики, С. Рехман

Дефекти соларног панела могу довести до значајног губитка ефикасности и повећаних трошкова одржавања. Конвенционалне методе откривања кварова су често споре и неефикасне. Ова студија поново разматра алгоритам You Only Look Once (YOLO) и његове варијације, процењујући њихову ефикасност у идентификацији недостатака у терм–ичким сликама соларних панела. Након тога, предс–тављамо нови YOLO алгоритам, назван YOLOS-PV, изграђен на YOLO алгоритму заснованом на трансформатору. Предложени алгоритам уводи тежине функције нових губитака да би одредио приоритет локализованих објеката и визуелизовао мапу пажње сваке главе трансформатора у оквиру YOLOS алгоритма. У експериментима, YOLOS-PV постиже мАП@0.5:0.95 резултат од 0.894, надма–шујући ефикасност других YOLOS варијанти. Имп–лементација кода се може наћи овде: tella26/IOLOS-PV (github.com).